Article

Coating Condition Detection and Assessment on the Steel Girder of a Bridge through Hyperspectral Imaging

Pengfei Ma [1], Jiaoli Li [1], Ying Zhuo [1], Pu Jiao [2] and Genda Chen[1,*]

[1] Missouri University of Science and Technology, Department of Civil, Architectural, and Environmental Engineering, Rolla, MO, USA
[2] University of Kentucky, Department of Computer Science, Lexington, KY, USA
* Correspondence: gchen@mst.edu

Abstract: The organic coating of bridge steel girders is subjected to physical scratches, corrosion, and aging in natural weathering. The breakdown of the coating may cause serviceability and safety problems if left unnoticed. A hyperspectral imaging method is proposed to detect the condition of steel coatings based on coating-responsive features in reflectance spectra. A field test was conducted on the real-world bridge which shows obvious signs of degradation. The hyperspectral signature enables an assessment of the coating health and defect severity. The results indicated that the coating scratch can be effectively located in the domain of a hyperspectral image and the scratch depth can be determined by mapping a scratch depth indicator (SDI=R532nm / R641nm). Rust sources and products in steel girders can be identified by the unique spectral signatures and the rust stains (and thus stain areas) scattered on the coating can be pinpointed at pixel level by the corrosion rust indicators. The chemical integrity of a topcoat is demonstrated by the short-wave infrared spectroscopy and the topcoat degradation can be evaluated by the absorption at 8000 cm^{-1} and 5850 cm^{-1}.

Keywords: steel girder; nondestructive inspection; corrosion; coating degradation; spectroscopic analysis; hyperspectral imaging

1. Introduction

Steel has been a candidate in civil engineering, especially in bridges because of its high strength and light weight. There are many uses of steel components in suspension, cable-stay, and girder bridges to overcome the self-weight problem [1-2]. It can also be used as a superstructure for arch bridges to facilitate the construction of the deck and undertake loads. For example, the Sydney Harbor Bay bridge [3]. In addition, steel is also widely used for girders in highway bridge networks (>30%) to provide more clearance for traffic [4]. However, steel components that are exposed to the natural weathering environment will be severely impaired by corrosive media and thus introducing safety and serviceability issues [4-5]. According to Federal Highway Administration (FHWA), statistics show that around 45% of steel bridges are structurally deficient with 19% being almost structurally obsolete [6]. Corrosion is currently the biggest concern for the structural integrity of steel components [7-8]. The deteriorated coating increased the chances of corrosion on the steel substrate [4]. Therefore, regular inspection is necessitated for coating and its conditions should be assessed to ensure acceptable serviceability to protect the substrate from directed contact with the corrosive factors [9].

Coatings are required to have protection against various degradations, physical or chemical [10]. The coating should be able to withstand physical impairment such as scratches, and abrasion as well as some aggressive species like chlorides, acids, and water [4, 9-10]. Coatings defects are thus different depending on degradation exposures [11]. Many aspects of the coatings can be monitored to assess the condition, such as delamination, chalking, checking, and rust staining [11-12]. Visual inspection has long been practiced for bridge coating due to its reliable inspection quality. However,

Preprints (www.preprints.org) | NOT PEER-REVIEWED | Posted: 3 May 2023 doi:10.20944/preprints202305.0121.v1

this method requires experienced practitioners, and the evaluation of coating condition assessment might be subjected to objective and quantifiable issues. Visual inspection is also time-consuming and labor-intensive, which makes it not possible in terms of regular inspection [13]. The electrochemical impedance spectroscopy (EIS) technique has been studied to detect the coating integrity as well as the substrate corrosion occurrence. Impedance values can effectively reflect the coating status before the presence of macroscopic degradations, but EIS does not give local information and thus a vague location of the impaired coating spots [14-15]. Spectroscopic techniques, Fourier transform infrared spectroscopy (FTIR), Raman Spectroscopy, and Mossbauer spectroscopy, have been performed to evaluate the coating conditions but generally are limited in the lab experiment [9, 17-18]. The image-based method has been implemented together with machine learning techniques over the last two decades to achieve fast inspection [19-20]. The pixel-level imagery features in conjunction with the artificial intelligence (AI) algorithm significantly improved the efficiency and reliability, which might be a substitute for human inspection [19, 21]. However, an apparent drawback is that RGB images are unable to provide information about the coating chemicals and thus an inability of a thorough assessment before the occurrence of the obvious defects [22]. In addition, it may confront some confusion in the detection if the defects are dominantly featured by color and the computer vision method is sensitive to the nonuniform illuminations on the detected surfaces [19].

Hyperspectral imaging (HSI) is emerging as a compromised tool for simultaneous spatial and spectral inspection because hyperspectral imaging possesses the RGB information and the surface composition information according to the response at different wavelengths [8, 24]. Therefore, both spatial dysconnectivity and compositional inhomogeneity can be plotted in the view of hyperspectral imaging [24]. The technique has been utilized to quantitatively assess the coating thickness of the paint on the steel according to the spectral signature as well as the discrimination of different chemical binders and polymers in the coating composition for automatic coating condition detection [25-26]. Likewise, the NIR spectroscopy was used to evaluate the conversion of white pigment of the acrylate coatings exposed to UV [27]. Hyperspectral imaging has also been tested to identify pinholes in the coating by introducing a matching filter at the pixel level [23]. To differentiate the colors from different objects in the girder coatings, Dayakar established an SVM model, and the color yellow from corrosion rust of different environments, acid or sulfate can be discriminated at a 94% accuracy [3]. Hyperspectral imaging was also practiced in an arch bridge truss coating assessment. The proposed multi-class Support Vector Machine (SVM) can generate highly accurate coating assessment results by integrating the information from only 21 bands in the range of the visible spectrum [28]. However, the application of hyperspectral imaging mainly focused on the characterization of coating degradations in lab. It is noted that the established method based on HSI for coating defects identification and condition assessment in real structures is not sufficient.

In this study, hyperspectral imaging is proposed to inspect the coatings on the steel girder of a real bridge. Some typical coating defects under natural weathering exposures are preselected for hyperspectral scanning to demonstrate their capability. The hyperspectral results are validated with the ground-truth lab characterizations, FTIR, scanning electron microscope (SEM), and energy dispersive X-ray spectroscopy (EDS), to illustrate the applicability of hyperspectral imaging technique in the coating condition detection and assessment. It is found that the coating scratch profiles can be detected, and the scratch depth is characterized by the spectral signatures of the coating layers and substrate. The chemically degraded coating can be distinguished from the sound coating by hyperspectral reflectance features in SWIR. In addition, the rust stains can be identified without color bias by hyperspectral imaging and the rust medium can be recognized according to the unique spectral signatures of rust products.

2. Materials and Methods

The proposed hyperspectral imaging technique for coating condition detection is demonstrated on a continuous girder bridge on the main road of 10th Street, Rolla, Missouri. The bridge is an eight-span steel girder bridge with a span configuration of 15.79 m, 15.54 m, 16.46 m, 18.59 m, 18.89 m, 12.49 m, 16.15 m, 11.85 m (total 125.5 m) from west to east. The steel used in the bridge girder is

Preprints (www.preprints.org) | NOT PEER-REVIEWED | Posted: 3 May 2023 doi:10.20944/preprints202305.0121.v1

fabricated structural carbon with a nominal yield strength of 20,000 psi. W30 and W33 steel girders were used for the continuous-span bridge to provide more clearance for the railway.

The bridge was constructed in 1974 and the steel girders were originally coated with brown lead silicochromate. The coating was removed in 2002 due to health concerns in terms of lead and was displaced by the current calcium sulfonate pigmented alkyd coating coupled with epoxy primer as shown in Figure 2. Calcium sulfonate alkyd paint is designed for replacement due to its significant corrosion inhabitation effect. This bridge was selected as the research object because of the presence of various typical coating detects on the girders. In addition, an alkyd topcoat is also one of the most widely used paints in current bridge protection [4].

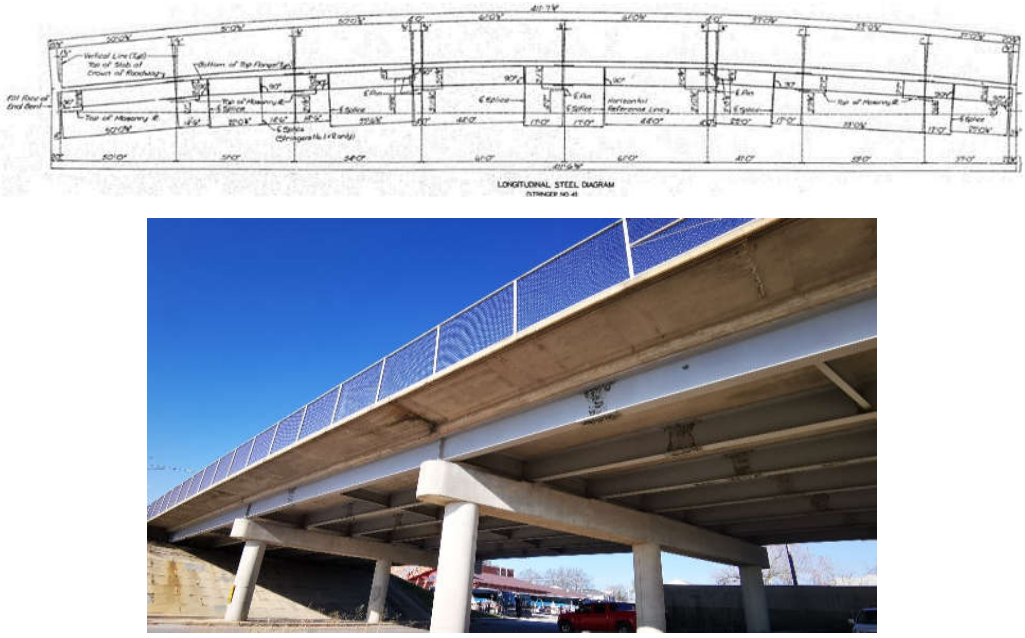

Figure 1. Elevation of the test bridge.

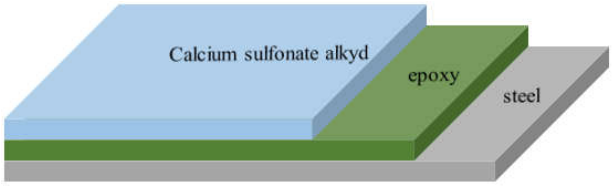

Figure 2. Coating system demonstration for the steel girder .

To characterize the coating defects with hyperspectral imaging, the preselected spots of interest (SOI) on the girder coating were scanned with a Headwall dual-len hyperspectral (Headwall phonetic, Massachusetts, USA) camera as shown in Figure 3. The camera has a 1.2 m standoff to the SOIs. Under the natural light radiation, the exposure time was set to 45 ms accordingly to prevent over-exposure in the hyperspectral image. The hyperspectral camera in this study enables the spectral range of visible and near-infrared (VNIR, 400-100 nm) and short-wave infrared (SWIR, 1000-2500 nm) with a spectral resolution of 2.21 nm in VNIR and 6.02 nm in SWIR. Prior to every HSI collection, the dark was captured with the cap on to reduce the internal current noise in the image. Likewise, white reference was also collected for the conversion of the raw digital numbers to radiance and finally reflectance. In this test, the camera was supported by a tripod because the SOIs are accessible otherwise the camera can be integrated into an unmanned aerial vehicle for coating inspection.

Preprints (www.preprints.org) | NOT PEER-REVIEWED | Posted: 3 May 2023 doi:10.20944/preprints202305.0121.v1

Figure 3. Setup for hyperspectral imaging collection in the field.

Hyperspectral imaging is indeed a subset of the spectroscopic technique for polymer characterization in this study. As the hyperspectral imaging in this study enables the wavenumbers from 4000 cm-1 to 10000 cm-1, it is featured by the band combinations, coupling, and overtones [27]. Therefore, FTIR is used to validate the hyperspectral results. Some coating samples are retrieved from the bridge for analysis. The FTIR spectra were recorded with a Nicolet™ iS50 FTIR Spectrometer in the spectral range between 400 cm−1 and 4000 cm−1 with a resolution of 4 cm−1. For each sample, 16 runs were performed to enhance the spectra and reduce the noise. The FTIR spectra are presented in transmittance for easy comparison in this study. In addition, scanning electron microscope (SEM) was performed on coating (rust-stained, healthy, degraded) samples using a Helios Hydra CX with an accelerating voltage of 15 kV and a beam current of 0.8 nA under high vacuum pressure (< 5.0E-4 Pa). The working distance between the lens and the sample was set to 4 mm. To determine the atomic distribution on the topcoat, EDS energy dispersive X-ray spectroscopy (EDS) was performed with a Thermo Noran Ultra Dry 60 mm2 detector by mapping in the Pathfinder X-Ray Microanalysis Software. As the organic coating in this study is nonconductive, all samples were coated with a thin film of gold/palladium (Au/Pd) by sputtering for 45 seconds to prevent charging.

3. Results and discussion

3.1. Coating scratch

Figure 4a presents the view of the coating scratch on the bridge steel girder. It is observed that the scratch depth varies along the trace as the scratch even reaches the undercoat in some areas. The coating thickness is reduced though the color difference from the original view is not significant. In addition, it is not known whether the substrate steel is exposed due to scratches. Coating is used to protect the steel from corrosive media. Corrosion can initiate at a bare steel spot and the effect gradually propagates concentrically to the local, which progressively damages the health coatings. Figure 4b shows the comparison of the spectral signatures in the range of 400-1000 nm (visible and near-infrared, VNIR) from different objects, topcoat (pigmented alkyd), undercoat (epoxy), and girder steel, in the domain of scratches from the hyperspectral imaging. In view of hyperspectral imaging, those three objects are spectrally different especially for the topcoat and undercoat though both are organic polymers that are characterized by aromatic rings and side chains. As for the substrate, steel does not yield any absorption features in the range of VNIR because the steel is composed of metal ions which do not absorb photons in the current wavelength domain [29].

Preprints (www.preprints.org) | NOT PEER-REVIEWED | Posted: 3 May 2023 doi:10.20944/preprints202305.0121.v1

To differentiate different layers of coating, scratch depth indicator (SDI) is developed by the ratio between two bands, 536 nm and 641 nm. Figure 5b displays the F-value results derived from the One-way ANOVA analysis based on the spectra from the three objects. There are two local maxima at 426 nm and 641 nm and one local minimum at 536 nm. According to ANOVA F-value, spectra at wavelength 536 nm yield the least variation ($p<0.05$) in the range of 400-750 nm. For comparison, 426 nm and 641 nm are more sensitive to the differences between different coating layers because higher close F-values are observed, which is around 21 ($p<0.05$). To establish a robust indicator, 641 nm is selected as the most sensitive band in this study because 426 nm is located at the beginning of the spectrum which is usually subjected to severe mechanical noises [8]. Figure 5a demonstrates the mapping of SDI (536 nm/641 nm) in hyperspectral imaging. The scratch profile can be easily identified, and the exposed undercoat can be located by the black spots. In order to assess the scratch condition, different layers of the coating are retrieved from the mapping by thresholds to demonstrate the scratch depth. The corresponding SDI threshold for undercoat and steel is obtained from the distribution of the SDI values as illustrated in Figure 5b and Figure 5d. For undercoat epoxy, the critical SDI 1.33 isolates the exposed undercoat though some scattered misidentifications can be observed. Most of the misclassifications of the undercoat are located in the shades of the white reference board. This is because the shade can distort the spectra and thus produce incorrect information, which can be eliminated by the additional external light source in real practices [24]. It is noted that several pixels are distinguished from the undercoat in the heart of scratch 'M', which is the substrate steel. As hyperspectral imaging also enables a high spatial resolution of 0.56 mm in this study, the exposed steel can be spotted by the critical SDI of 0.95. There are in total 5 pixels that can be identified, which makes a 1.57 mm2 exposure. It is worth noting that hyperspectral imaging can perform a much more accurate inspection by using spectral information compared to the RGB inspection.

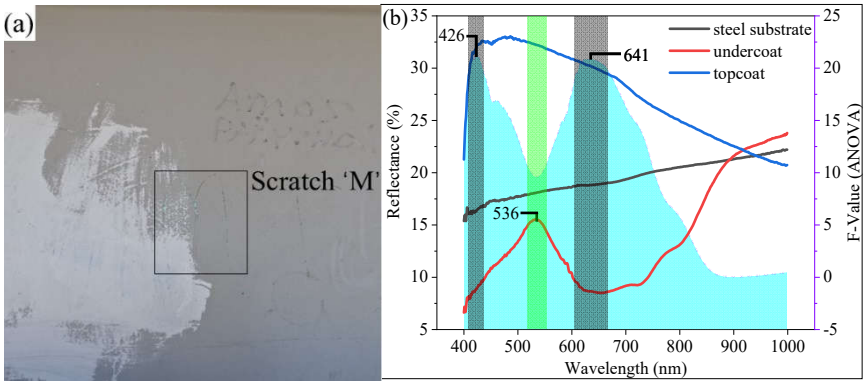

Figure 4. Coating scratch on the steel girder (a) original view, (b) spectral signatures of different coating layers and the corresponding F-values from ANOVA analysis of spectra.

Preprints (www.preprints.org) | NOT PEER-REVIEWED | Posted: 3 May 2023 doi:10.20944/preprints202305.0121.v1

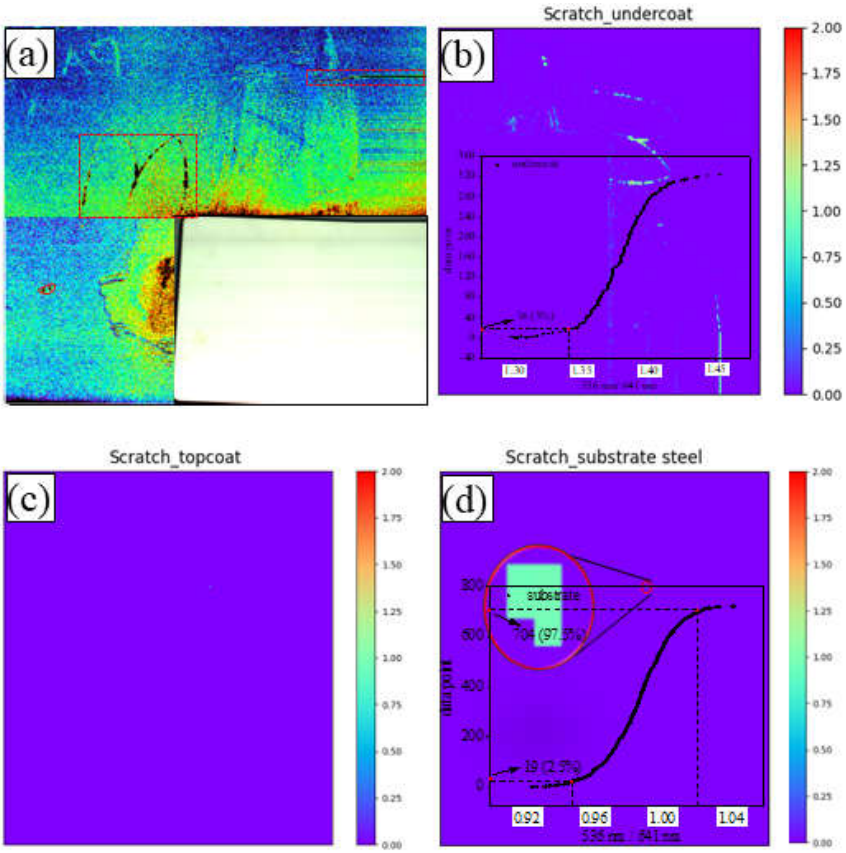

Figure 5. Different layers of the girder coating with scratches (a) mapping of SDI (536 nm/641 nm) in hyperspectral imaging, (b) scratch of undercoat (SDI>1.33), (c) scratch of substrate steel (0.95<SDI<1.02), (d) topcoat otherwise.

3.2. Steel rust stains

All figures and tables should be cited in the main text as Figure 1, Table 1, etc. Steel rust percentage has been used as an indicator to assess the coating conditions according to ASTM so as for timely remedies [28]. Figure 6 presents the coating surface with steel rust stains as well as the corroded steel girder top flange. Many corrosive media cause rust in the atmospheric environment and the corrosion products may vary. Acidic exposures are prone to produce Fe3O4 (magnetite), FeCl2 (ferrous chloride), and FeOOH [30]. For chloride salt ions attack, β-FeOOH (akageneite) and α-FeOOH (goethite) are the main corrosion products [30-31]. Two steel plates with the treatment of sodium chloride and water respectively are prepared and placed in the view of the scanning view. Figure 6b shows the spectral signatures in the VNIR range derived from corrosion spots on two plates. It is noted that the rust products with different exposures differ spectrally. Rust obtained from sodium chloride solution yields three absorption features at 612 nm, 733 nm, and 841 nm and water-based corrosion products have the features at 708 nm and 950 nm which is characterized by the water [8].

As chloride corrosion is more aggressive, it is worth emphasizing its corrosion effect before the pervasive attack on both substrate and organic coatings [14]. The chloride rust (CR) indicator, 733 nm / 841 nm, is constructed to demonstrate the corrosion products. Figure 6c demonstrates the mapping of CR in the domain of hyperspectral imaging with a threshold of 1.11. This critical CR is obtained from the stain pixels in the diaphragm with the same method as illustrated in SDI. The severely rusted steel flanges can be identified in CR mapping as indicated by the dark red areas. Moreover, the rust stain on the coating in the diaphragm is also detected by the CR though the CR values are smaller compared to the rust spots. It is because rust products intermingle with the topcoat in the domain of a pixel. The hyperspectral spectrum is representative of the overall composition of the chemicals in that pixel [8].

Preprints (www.preprints.org) | NOT PEER-REVIEWED | Posted: 3 May 2023 doi:10.20944/preprints202305.0121.v1

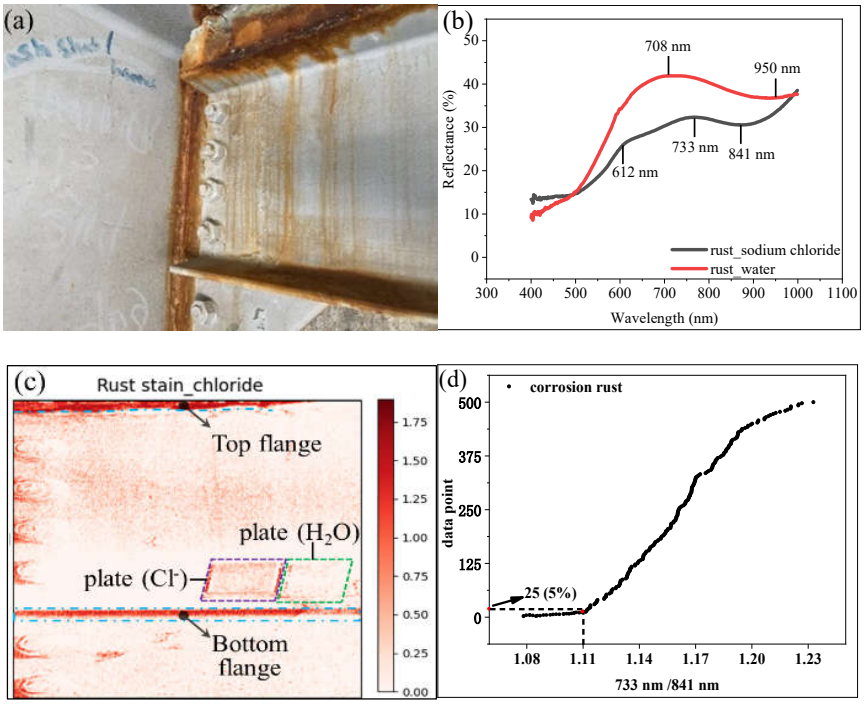

Figure 6. Girder coating with rust stain (a) the view of the rust spot, (b) spectral signatures of the different rust products in VNIR, (c) rust stain demonstration by CR indicator (>1.11), (d) critical CR for rust stain on topcoat.

The coating samples with rust stains are analyzed by the energy dispersive X-ray spectroscopy (EDS) as opposed to the normal coating on this girder, Figure 7 shows the comparison of the element mapping results. The EDS spectrum as shown in Figure 7a demonstrates detectable peaks in terms of Cl for the rust-stained coating while the rust-free coating is dominated by the topcoat polymer compositional elements, C and O. The presence of Cl is also reflected by the element mapping result as illustrated in Figure 7b. For elements related to steel rust, Fe and Cl show significant differences in distribution. Oxygen (O) is not considered here to distinguish rust because of its massive existence in alkyd resins and thus cannot be easily impacted. As seen from Figure 7b, Fe is more visible on the coating with rust stains though Fe is also spotted in the rust-free coating samples. For Cl, the contrast is more significant because it almost disappears in rust-free samples. Table 1 shows the element ratio of each detectable element present on the coating surface. C and O occupy, in total, about 90% and N is the third prevailing element that makes up around 7.5% of the coating topology. The element dominance agrees well with the composition of alkyd. Rust-stained coating sees Fe of 1.78% which is higher than the 0.56% in the rust-free coating. As for Cl, it occupies 0.51% of the total detectable elements for the topcoat with rust stains in comparison with the 0% Cl in the stain-free topcoat. Element Cl distinguishes the rust-contaminated coatings from the rust-free sample which shows negligible presence. The result is consistent with the hyperspectral imaging result which shows the rust stain distribution as well as the corrosion source is Cl-related media.

Preprints (www.preprints.org) | NOT PEER-REVIEWED | Posted: 3 May 2023 doi:10.20944/preprints202305.0121.v1

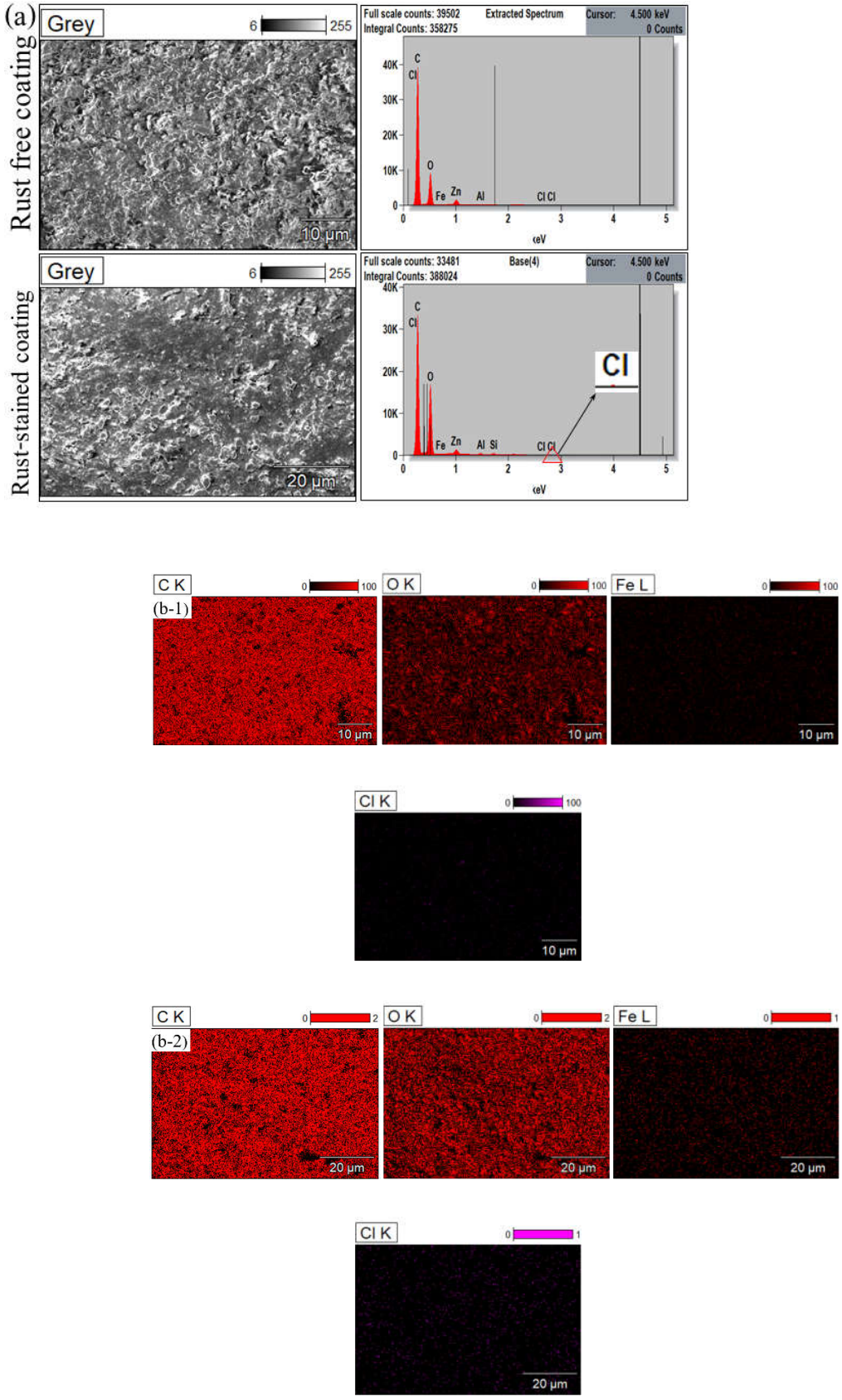

Figure 7. Comparison of the element distribution on the coating with and without rust stains by (a) EDS spectra, (b-1) EDS mapping of rust-free topcoat, (b-2) EDS mapping of rust-stained topcoat.

Preprints (www.preprints.org) | NOT PEER-REVIEWED | Posted: 3 May 2023 doi:10.20944/preprints202305.0121.v1

Table 1. Percent of the detachable elements on the coating with and without rust stain.

Element	C	O	N	Fe	Cl	Al	Zn
Rust-free coating	54.34	36.00	7.31	0.56	0	0.48	1.31
Rust-stained coating	53.15	34.98	7.43	1.78	0.51	0.38	1.53

3.3. Degraded topcoat

A degraded topcoat can expose the undercoat and thus increases the corrosion probability of the substrate. Early detection can potentially enhance the serviceability of steel girders. Figure 8 shows the deteriorated topcoat on the bottom flange of the steel girders in the proposed field bridge. Those deteriorated topcoats have lost the cling to the undercoat and thus cannot effectively protect the undercoat and substrate. As the degradation is generally characterized by chain breakage due to oxidation, Figure 9 displays the comparison between healthy and degraded topcoats by both FTIR and SWIR spectroscopy from hyperspectral imaging. FTIR is the complementary information for SWIR spectroscopy to interpret the topcoat degradation in view of the binder's chemical connections.

Considering the natural aging and atmospheric exposure effect on the topcoat, the stretching vibration of the C=O at 1726 cm-1 and C-O-C at 1528 cm-1 are featured by the bond cleavage in the polyester of the girder topcoat, alkyd resin [32-33]. Table 2 summarizes the band assignment of the alkyd resin. It can be seen that the narrow absorption bands at 1726 cm-1 and 1528 cm-1 both significantly decrease for the degraded topcoat in comparison to the healthy, which indicates the chains shortening in the polymer [33]. The chain scission in polyester is also observed by the decreasing absorption at 2920 cm-1 and 2850 cm-1 for degraded topcoat, which illustrates the reduced presence of the side chains [34]. In addition, the O-C-O featured band at 1410 cm-1 almost disappears to demonstrate the reduction side chain [35]. On the contrary, it is noted that 1635 cm-1 is boosted due to the degradation effect on the topcoat [33, 36]. It is because of the autooxidation of the polymer crosslink. In this process, the degraded alkyd resin releases alcohol and carbonyl species, which thus reduces the molecular weight of the original topcoat component [34]. The decreasing weight of alkyd resin can also be implied by the diminished bands at 1100 cm-1 and 1252 cm-1. The breakage of C-O-C produces volatile species, for example, phthalic acid due to the Norrish Type I reaction [33]. Figure 10 shows the microstructure of the healthy and deteriorated topcoat by SEM. In comparison, the degraded topcoat yields a messier topology, and the topcoat has been degraded into more pieces. Table 3 illustrates the presence of detectable elements on the topcoat derived from the EDS mapping results. C is significantly reduced from the healthy to degraded topcoat due to the oxidation effect, which conforms to the FTIR results.

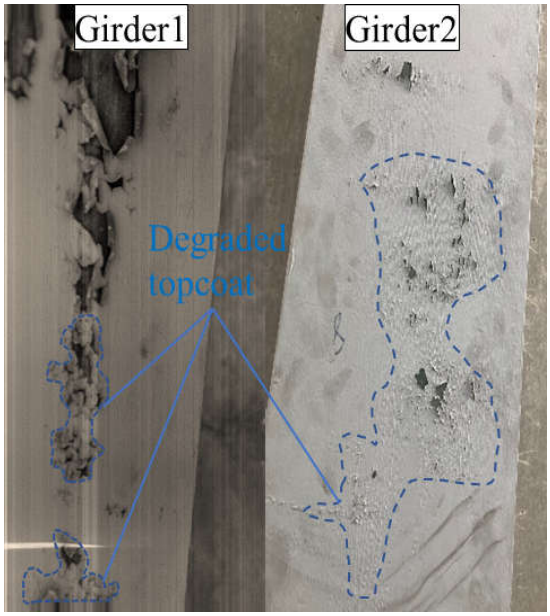

Figure 8. Demonstration of the degraded topcoat on the bottom flange of the steel girder.

Preprints (www.preprints.org) | NOT PEER-REVIEWED | Posted: 3 May 2023 doi:10.20944/preprints202305.0121.v1

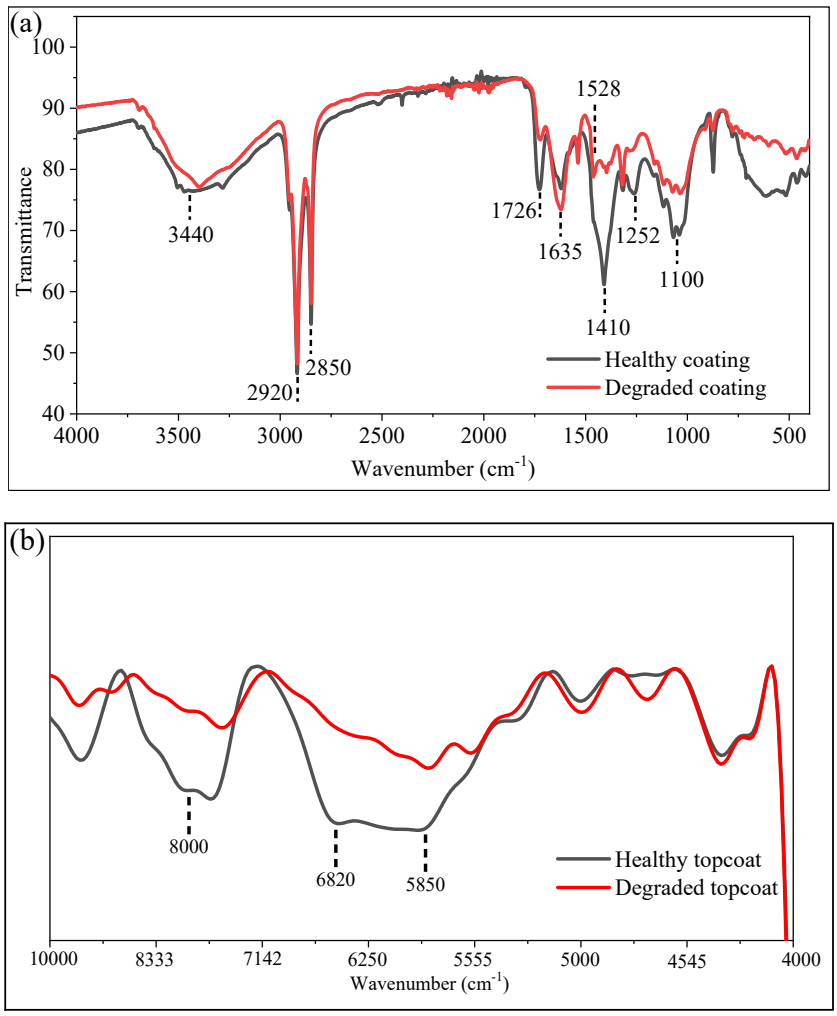

Figure 8. Comparison of the healthy and degraded topcoat in the range of (a) 400-4000 cm-1 (FTIR), (b) 4000-10000 cm^{-1} (SWIR).

Table 2. Major bands of Alkyd resin in FTIR and its band assignment.

Wavenumber (cm^{-1})	Assignment
741-705	aromatic out-of-plane bending
<1000	ring vibrations and C-X (with X = Cl or CH_3) coupling
1070	aromatic in-plane bending
1119	C-O-C stretching
1258	C-O-C stretching
1340-1300	vibrations involving the aromatic rings
1429	O-C-O bending
1528	C-O-C bending
1590	aromatic in-plane bending
1650-1500	C=N, C=O
1635	C=C stretching
1726	C=O stretching vibration carboxylic acids and esters
2850	(C-H)-CH_2 symmetric stretching
2921	(C-H)-CH_2 asymmetric stretching
3440/3314	OH stretching

Figure 10b presents the spectra derived from the healthy and the degraded topcoat in the range of 4000-10000 cm-1 after continuum removal processing to facilitate quantitative comparison [37-38]. As illustrated in the FTIR, the main and side chains were greatly shortened due to the degradation effect. The reduction of the C=O in the degraded topcoat can also be detected in SWIR spectroscopy

Preprints (www.preprints.org) | NOT PEER-REVIEWED | Posted: 3 May 2023 doi:10.20944/preprints202305.0121.v1

by the carbonyl stretching characterized bands at 5850 cm^{-1} [39]. This band should be the overtones of the fundamental vibration of the carbonyl groups illustrated in 400-2000 cm^{-1}. A similar decreasing trend at 5850 cm^{-1} is also observed on the alkyd resins under ultra-violate exposure [39]. Another significant difference is located around 6820 cm^{-1}, characterized by the second overtone of the hydroxyl group [8, 40]. The absorption feature is almost erased due to the deterioration of the topcoat. The deletion of hydroxyl groups is also observed by the absorption at 3440 cm^{-1} [33-34]. However, band 3440 cm^{-1} remains significant though decreased. It is because 3440 is featured by not only the bending vibration of hydroxyl but also water [8]. The third recognizable spectral zone that differentiates healthy and degraded topcoats is around 8000 cm^{-1}. This absorption intensity of this broadband shrinks due to the degradation of the topcoat, which is attributed to the loss of the oxygenated products, singly- doubly-bonded oxygen, due to photooxidation [39]. 000-10000 cm^{-1} (SWIR).

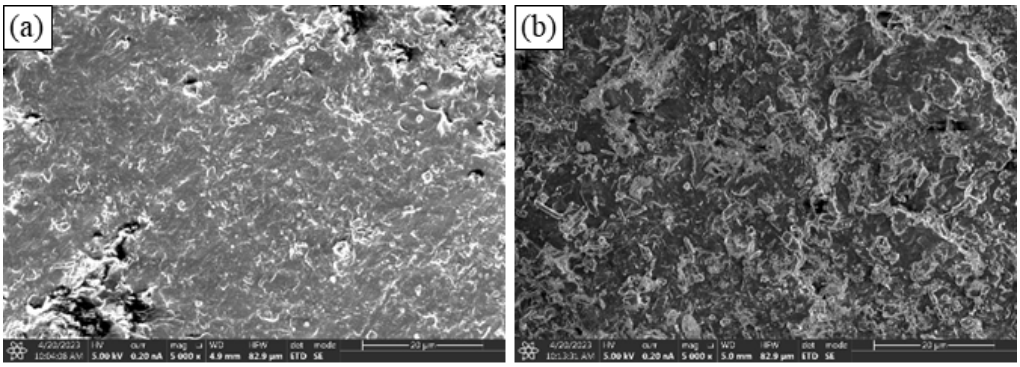

Figure 10. Topology by SEM of (a) healthy topcoat, (b) degraded topcoat.

Table 3. Percentage of the detachable elements on the coating with and without rust stains.

Element	C	O	N	Fe	Cl	Al	Zn
Healthy topcoat	53.15	37.53	7.43	0.43	0	0.52	1.37
Degraded topcoat	42.19	48.47	7.58	0.25	0	0	1.50

4. Conclusions

The study presents a study that uses hyperspectral imaging to detect the coating defects in bridge steel girders. The results and discussion show that the coating scratch profiles can be effectively depicted, and the scratch depth can be exactly identified by the scratch indicators derived by the spectral bands derived from the ANOVA analysis of spectral signatures of different coating layers. In addition, the rust-stained coating can be estimated by the corrosion rust indicators and the corrosion source can be evaluated due to the diagnostic absorption features of rust products in the range of VNIR. As for the degraded topcoat, SWIR spectra show significant reduction at 8000 cm^{-1}, 5850 cm^{-1} as well as the hydroxyl absorption at 6820 cm^{-1}.

For a more robust inspection of the girder coatings, further work should focus on the quantitative study of how the SWIR spectra can evaluate the severity of the coating degradations. And more types of industrial coatings need to be tested with hyperspectral imaging to determine the corresponding indicator to differentiate its presence from other layers, which can greatly expand the application of hyperspectral imaging in fast nondestructive inspection of the girder coating conditions.

Author Contributions: Conceptualization, methodology, investigation, writing original draft preparation, P.M.; methodology, investigation, J.L.; methodology, Y.Z., and P.J.; review and funding acquisition, G.C.

Funding: Financial support to complete this study was provided by the US Department of Transportation, Office of the Assistant Secretary for Research and Technology (USDOT/OST-R) under Grant No. 69A3551747126 through the INSPIRE University Transportation Center (https://inspire-utc.mst.edu) at Missouri University of

Science and Technology. The views, findings, and conclusions reflected in this publication are solely those of the authors and do not represent the official policy or position of the USDOT/OST-R, or any state or other entity.

Acknowledgments: The authors wish to thank Ibrahim Alomari and Peter Ogunjinmi for their assistance during hyperspectral data collection at the bridge site.

Conflicts of Interest: The authors declare no conflict of interest.

References

1. Kitada, T., 2006. Considerations on recent trends in, and prospects of, steel bridge construction in Japan. Journal of Constructional Steel Research, 62(11), pp.1192-1198. https://doi.org/10.1016/j.jcsr.2006.06.016
2. M, P., An, J., Zhang, B., Zhu, P., Zhao, H., 2020. Research on Axle Load Recognition Algorithm Based on U-rib Transverse Influence Line. Highway Engineering, 45(5), 9 https://doi.org/10.19782/j.cnki.1674-0610.2020.05.001
3. Mustapha S, Huynh CP, Runcie P, Porikli F. Paint condition assessment of civil structures using hyper-spectral imaging. In: SHMII 2015 - 7th International Conference on Structural Health Monitoring of Intelligence Infrastructure. Intl Society for Structural Health Monitoring of Intelligence Infrastructure; 2015.
4. Yanez, L.M.M., 2016. Bridge maintenance to enhance corrosion resistance and performance of steel girder bridges (Doctoral dissertation, Purdue University).
5. Zhang, L., Lv, X., Lau, K., Viswanathan, S., Li, M. and Gosain, P., 2021. Assessment of Structural Steel Coating Applications.
6. FHWA, (2015). USDOT. "Bridges and Structures – Bridges by Year Built 2013". Federal Highway Administration. US. Department of Transportation. http://www.fhwa.dot.gov/bridge/structyr.cfm (accessed 20 April 2023).
7. Menga, A., Kanstad, T., Cantero, D., Bathen, L., Hornbostel, K. and Klausen, A., 2023. Corrosion-induced damage and failures of posttensioned bridges: A literature review. Structural Concrete, 24(1), pp.84-99. https://doi.org/10.1002/suco.202200297
8. Ma, P., Fan, L. and Chen, G., 2023. Hyperspectral reflectance for determination of steel rebar corrosion and Cl− concentration. Construction and Building Materials, 368, p.130506. https://doi.org/10.1016/j.conbuildmat.2023.130506
9. Cook, D.C., 2005. Spectroscopic identification of protective and non-protective corrosion coatings on steel structures in marine environments. Corrosion Science, 47(10), pp.2550-2570. https://doi.org/10.1016/j.corsci.2004.10.018
10. Chong, S.L., 1997. A Comparison of Accelerated Tests for Steel Bridge Coatings in Marine Environments. Journal of Protective Coatings & Linings, 14(3). http://worldcat.org/issn/87551985
11. Liao, K.W. and Lee, Y.T., 2016. Detection of rust defects on steel bridge coatings via digital image recognition. Automation in Construction, 71, pp.294-306. https://doi.org/10.1016/j.autcon.2016.08.008
12. Corrosionpedia, Coating Failures and Defects. https://www.ppcoatings.co.uk/wp-content/uploads/2016/06/Coating-Failure-Defects.pdf, 2016
13. Yao, Y., Kodumuri, P. and Lee, S.K., 2011. Performance evaluation of one-coat systems for new steel bridges (No. FHWA-HRT-11-046). United States. Department of Transportation. Federal Highway Administration.
14. Waters, N., Connolly, R., Brown, D. and Laskowski, B., 2014. Electrochemical impedance spectroscopy for coating evaluation using a micro sensor. In Annual Conference of the PHM Society (Vol. 6, No. 1). https://doi.org/10.36001/phmconf.2014.v6i1.2340
15. Hayashibara, H., Tada, E. and Nishikata, A., 2017. Monitoring the early stage of degradation of epoxy-coated steel for ballast tank by electrochemical impedance spectroscopy. Materials transactions, 58(12), pp.1687-1694. https://doi.org/10.2320/matertrans.M2017243
16. Kanbayashi, T., Ishikawa, A., Matsunaga, M., Kobayashi, M. and Kataoka, Y., 2019. Application of confocal raman microscopy for the analysis of the distribution of wood preservative coatings. Coatings, 9(10), p.621. https://doi.org/10.3390/coatings9100621
17. Müller, J., Knop, K., Thies, J., Uerpmann, C. and Kleinebudde, P., 2010. Feasibility of Raman spectroscopy as PAT tool in active coating. Drug development and industrial pharmacy, 36(2), pp.234-243. https://doi.org/10.3109/03639040903225109
18. Hayes, P.A., Vahur, S. and Leito, I., 2014. ATR-FTIR spectroscopy and quantitative multivariate analysis of paints and coating materials. Spectrochimica Acta Part A: Molecular and Biomolecular Spectroscopy, 133, pp.207-213. https://doi.org/10.1016/j.saa.2014.05.058
19. Potenza, F., Rinaldi, C., Ottaviano, E. and Gattulli, V., 2020. A robotics and computer-aided procedure for defect evaluation in bridge inspection. Journal of Civil Structural Health Monitoring, 10, pp.471-484. https://doi.org/10.1007/s13349-020-00395-3
20. Feroz, S.; Abu Dabous, S. UAV-Based Remote Sensing Applications for Bridge Condition Assessment. Remote Sens. 2021, 13, 1809. https://doi.org/10.3390/rs13091809

21. Li, Y., Kontsos, A. and Bartoli, I., 2019. Automated rust-defect detection of a steel bridge using aerial multispectral imagery. Journal of Infrastructure Systems, 25(2), p.04019014. https://doi.org/10.1061/(ASCE)IS.1943-555X.0000488
22. Chen, M., Lu, G. and Wang, G., 2022. Discrimination of Steel Coatings with Different Degradation Levels by Near-Infrared (NIR) Spectroscopy and Deep Learning. Coatings, 12(11), p.1721. https://doi.org/10.3390/coatings12111721
23. Garrett, J.L., Johansen, T.A., Orlandić, M., Bashir, M.A. and Raeissi, B., 2021, March. Detecting Pinholes in Coatings with Hyperspectral Imaging. In 2021 11th Workshop on Hyperspectral Imaging and Signal Processing: Evolution in Remote Sensing (WHISPERS) (pp. 1-5). IEEE. https://doi.org/10.1109/WHISPERS52202.2021.9483974
24. Sandak, J., Sandak, A., Legan, L., Retko, K., Kavčič, M., Kosel, J., Poohphajai, F., Diaz, R.H., Ponnuchamy, V., Sajinčič, N. and Gordobil, O., 2021. Nondestructive evaluation of heritage object coatings with four hyperspectral imaging systems. Coatings, 11(2), p.244. https://doi.org/10.3390/coatings11020244
25. Dingemans, L.M., Papadakis, V.M., Liu, P., Adam, A.J. and Groves, R.M., 2017. Quantitative coating thickness determination using a coefficient-independent hyperspectral scattering model. Journal of the European Optical Society-Rapid Publications, 13(1), pp.1-12. https://doi.org/10.1186/s41476-017-0068-2
26. Dingemans, L.M., Papadakis, V.M., Liu, P., Adam, A.J. and Groves, R.M., 2017. Quantitative coating thickness determination using a coefficient-independent hyperspectral scattering model. Journal of the European Optical Society-Rapid Publications, 13(1), pp.1-12. https://doi.org/10.1186/s41476-017-0068-2
27. Daikos, O., Heymann, K. and Scherzer, T., 2018. Monitoring of thickness and conversion of thick pigmented UV-cured coatings by NIR hyperspectral imaging. Progress in Organic Coatings, 125, pp.8-14. https://doi.org/10.1016/j.porgcoat.2018.08.022
28. Huynh, C.P., Mustapha, S., Runcie, P. and Porikli, F., 2015. Multi-class support vector machines for paint condition assessment on the Sydney Harbour Bridge using hyperspectral imaging. Struct. Monit. Maint, 2(3), pp.181-197. http://dx.doi.org/10.12989/smm.2015.2.3.000
29. Greenler, R.G., 1966. Infrared study of adsorbed molecules on metal surfaces by reflection techniques. The Journal of Chemical Physics, 44(1), pp.310-315. https://doi.org/10.1063/1.1726462
30. Lavadiya, D.N., Sajid, H.U., Yellavajjala, R.K. and Sun, X., 2022. Hyperspectral imaging for the elimination of visual ambiguity in corrosion detection and identification of corrosion sources. Structural Health Monitoring, 21(4), pp.1678-1693. https://doi.org/10.1177/14759217211041690
31. De Kerf, T., Pipintakos, G., Zahiri, Z., Vanlanduit, S. and Scheunders, P., 2022. Identification of corrosion minerals using shortwave infrared hyperspectral imaging. Sensors, 22(1), p.407. https://doi.org/10.3390/s22010407
32. Kızılkonca, E. and Erim, F.B., 2019. Development of anti-aging and anticorrosive nanoceria dispersed alkyd coating for decorative and industrial purposes. Coatings, 9(10), p.610. https://doi.org/10.3390/coatings9100610
33. Anghelone, M., Stoytschew, V., Jembrih-Simbürger, D. and Schreiner, M., 2018. Spectroscopic methods for the identification and photostability study of red synthetic organic pigments in alkyd and acrylic paints. Microchemical Journal, 139, pp.155-163. https://doi.org/10.1016/j.microc.2018.02.029
34. Anghelone, M., Jembrih-Simbürger, D. and Schreiner, M., 2016. Influence of phthalocyanine pigments on the photo-degradation of alkyd artists' paints under different conditions of artificial solar radiation. Polymer Degradation and Stability, 134, pp.157-168. https://doi.org/10.1016/j.polymdegradstab.2016.10.007
35. Duce, C., Della Porta, V., Tiné, M.R., Spepi, A., Ghezzi, L., Colombini, M.P. and Bramanti, E., 2014. FTIR study of ageing of fast drying oil colour (FDOC) alkyd paint replicas. Spectrochimica Acta Part A: Molecular and Biomolecular Spectroscopy, 130, pp.214-221. https://doi.org/10.1016/j.saa.2014.03.123
36. Christensen, P.A., Dilks, A., Egerton, T.A., Lawson, E.J. and Temperley, J., 2002. Photocatalytic oxidation of alkyd paint films measured by FTIR analysis of UV generated carbon dioxide. Journal of materials science, 37, pp.4901-4909. https://doi.org/10.1023/A:1020882701724
37. Zahiri, Z., Laefer, D. F., & Gowen, A., 2018. The feasibility of short-wave infrared spectrometry in assessing water-to-cement ratio and density of hardened concrete. Construction and Building Materials, 185, 661-669. https://doi.org/10.1016/j.conbuildmat.2018.07.082
38. Daikos, O., Heymann, K. and Scherzer, T., 2018. Monitoring of thickness and conversion of thick pigmented UV-cured coatings by NIR hyperspectral imaging. Progress in Organic Coatings, 125, pp.8-14. https://doi.org/10.1016/j.porgcoat.2018.08.022
39. Miller, C.D., 1958. Kinetics and Mechanism of Alkyl Photooxidation. Industrial & Engineering Chemistry, 50(1), pp.125-128.
40. Fan, L., Fan, M., Alhaj, A., Chen, G. and Ma, H., 2020. Hyperspectral imaging features for mortar classification and compressive strength assessment. Construction and Building Materials, 251, p.118935. https://doi.org/10.1016/j.conbuildmat.2020.118935